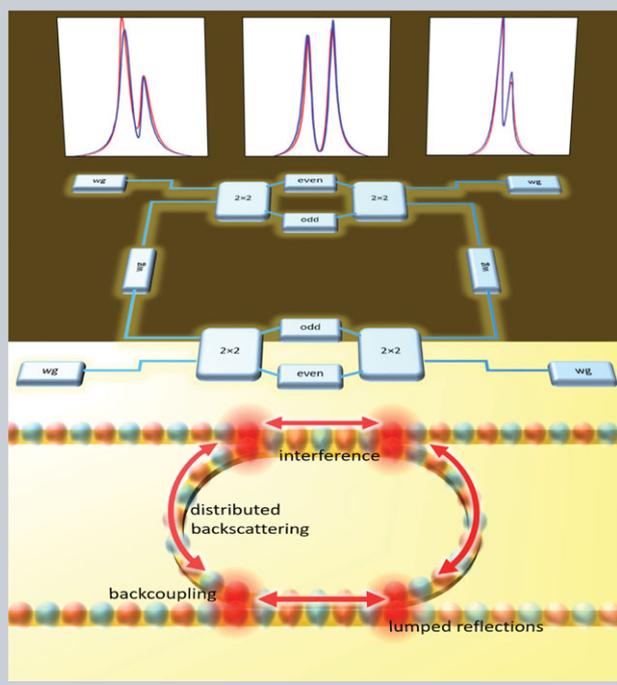ORIGINAL PAPER

Abstract Silicon microring resonators very often exhibit resonance splitting due to backscattering. This effect is hard to quantitatively and predicatively model. This paper presents a behavioral circuit model for microrings that quantitatively explains the wide variations in resonance splitting observed in experiments. The model is based on an in-depth analysis of the contributions to backscattering by both the waveguides and couplers. Backscattering transforms unidirectional microrings into bidirectional circuits by coupling the clockwise and counterclockwise circulating modes. In high-Q microrings, visible resonance splitting will be induced, but, due to the stochastic nature of backscattering, this splitting is different for each resonance. Our model, based on temporal coupled mode theory, and the associated fitting method, are both accurate and robust, and can also explain asymmetrically split resonances. The cause of asymmetric resonance splitting is identified as the backcoupling in the couplers. This is experimentally confirmed and its dependency on gap and coupling length is further analyzed. Moreover, the wide variation in resonance splitting of one spectrum is analyzed and successfully explained by our circuit model that incorporates most linear parasitic effects in the microring. This analysis uncovers multi-cavity interference within the microring as an important source of this variation.

Backscattering in silicon microring resonators: a quantitative analysis

Ang Li[1,2,*], **Thomas Van Vaerenbergh**[1,2,3], **Peter De Heyn**[4], **Peter Bienstman**[1,2], **and Wim Bogaerts**[1,2,5]

1. Introduction

Microring resonators are extremely useful devices to create compact wave-division-multiplexing (WDM) filters, (bio)sensors, all-optical signal processing, optical switches, optical wavelength converters, microwave photonics and laser cavities [1–7]. The use of silicon gives a high refractive-index contrast, allowing for ultra-compact rings with a large free spectral range (FSR). In addition, the material system is compatible with CMOS manufacturing processes, offering a route towards large-scale integration and mass manufacturing.

The basic operation principles of (silicon) microring resonators have already been described extensively [8, 9]. Basically, an ideal add–drop ring filter operates as shown in Fig. 1a. Light coupled from the *in* port circulates *clockwise* (CW) in the ring waveguide in one direction and gets

extracted at the *drop* port when the wavelength is near the resonance wavelength, or is coupled back to the *pass* port at other wavelengths. The transmission spectra at the *drop* and *pass* ports consist of a series of Lorentzian-shaped resonances, with no light coming out of the *add* and *in* ports, as evident in Fig. 2a. In this unidirectional behavior the *counterclockwise* (CCW) mode is never excited.

However, any non-ideality in the ring can lead to small backscattering that can excite the CCW mode. Especially near resonance, when the optical intensity in the ring waveguide is high, backscattering can lead to a coherent build-up of this reflected light, even if the individual reflections are very weak. This excitation of the CCW mode results in undesired power output at the *add* and *in* ports, and a perturbation of the ideal single-resonance state. The backscattering couples the degenerate CW and CCW modes into two new resonance states with a mixed CW/CCW nature and

[1] Photonics Research Group, Ghent University–IMEC, Ghent 9000, Belgium
[2] Center for Nano- and Biophotonics (NB-photonics), Ghent University, Ghent, Belgium
[3] Hewlett Packard Labs, 1501 Page Mill Road, Palo Alto, CA 94304, USA
[4] IMEC, Kapeldreef 75, Leuven, Belgium
[5] Luceda Photonics, Dendermonde, Belgium
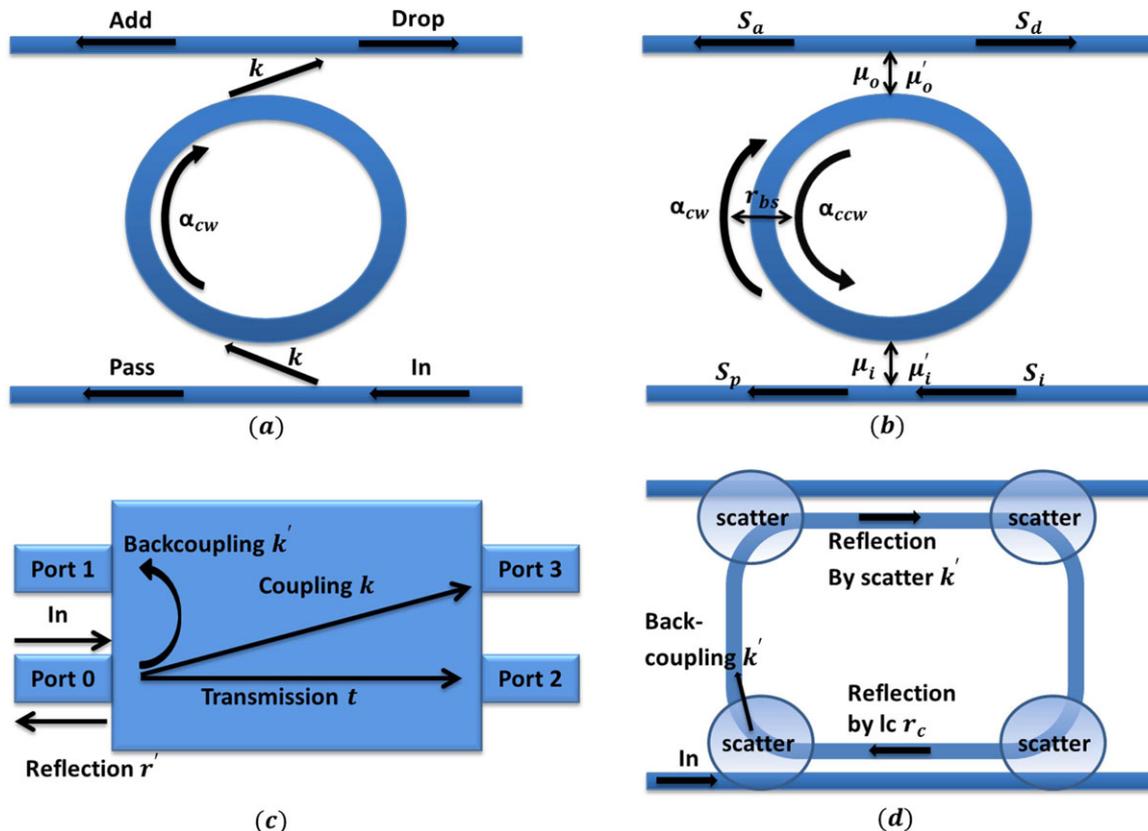*Corresponding author: e-mail: ang.li@intec.ugent.be

Figure 1 (a) Schematic of an ideal ring resonator without backscattering. Light coupled from the *in* port will circulate in the ring and be extracted from the *drop* port near the resonance wavelength, or continue to the *pass* port at other wavelengths. (b) t-CMT model for the ring with backscattering. Without backscattering, CCW and CW modes are degenerate in ring resonators; only one is excited by its corresponding input. However, as long as backscattering r_{bs} exists, the degeneracy is broken and they are coupled with each other. The factors μ_x, μ_x' stand for the mutual coupling of the directional couplers. (c) A simplified schematic of a 2×2 directional coupler. Ideally, the backcoupling k' and reflection r' are zero. (d) Illustration of the extra reflections caused by directional couplers. The directional coupler in a ring resonator can be physically divided into three parts, two scattering centers at the beginning and ending sections, and a distributed scatterer in the straight section due to extra coupling length. Scatterers will cause unwanted backcoupling to an adjacent port as well as reflection to the *in* port, while coupling length will bring roughness-induced backscattering.
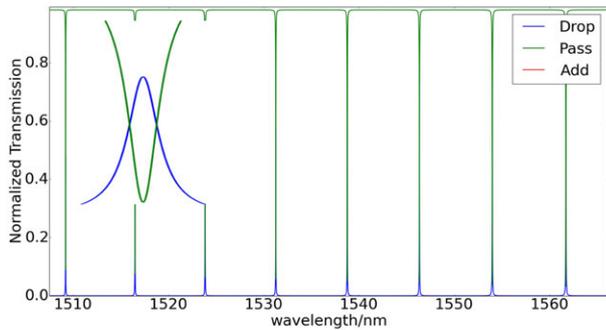
different resonance wavelengths. In rings with a very high Q factor, i.e. sufficiently narrow bandwidth, a visible resonance splitting in the spectral response will be induced, and the ring characteristics can be seriously deteriorated compared to the ideal case [10]. The backscattering can have many physical contributions, which means that it is also wavelength dependent; therefore, the resonance splitting can vary from one resonance to the next. This is shown in Fig. 2b, which is taken from a typical measurement of silicon microring resonators, and in Fig. 3, which shows the distributions of split ratios of six sets of ring resonators. Each set contains seven rings with variable lengths. This resonance splitting will cause problems for many ring resonator applications.

- In ring-resonator-based sensors, the shift of the resonance wavelength might not be correctly detected [11].
- In ring-resonator-based tunable lasers, the reflection at the *in* port as well as the distortion of the ring's transmission spectrum may cause laser instabilities.
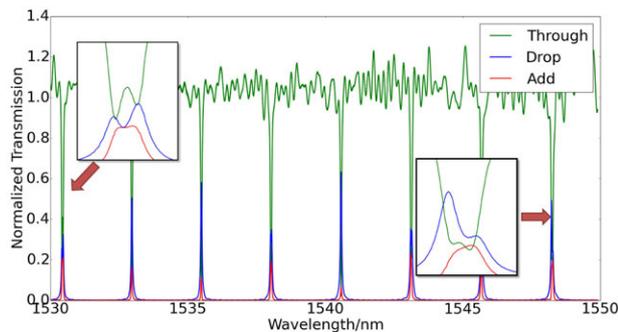
- In ring-resonator-assisted loss characterization techniques, wrong model parameters will be extracted from an imperfect fitting of split resonances [12].
- Ring-resonator-based WDM filters will deviate from the designed filter specifications, as the Q factor cannot be fully controlled.
- Ring-assisted microwave detection circuits could fail to get the correct peak power from a split resonance [6].

However, in some situations, the backscattering and resonance splitting in ring resonators can be harnessed and provide attractive benefits: for instance, the extinction ratio of a filter can be strengthened [13].

In order to correctly deal with such split resonances, and to either avoid or take advantage of backscattering, an accurate and robust model of the ring resonator with backscattering is required. Existing models do not adequately describe the observed features in optical measurements of microrings. Current fitting models typically describe only symmetrically split resonances [12–15]. No published models

(a) A spectrum of an ideal ring resonator. Clean Lorentzian-shaped resonances at *drop* and *pass* ports, no light at *in* and *add* ports.

(b) A measured spectrum of a silicon ring resonator. Resonances exhibit different shapes due to splitting.

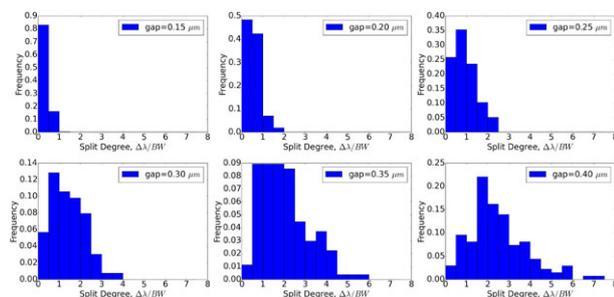**Figure 2** Examples of spectra of ideal and real ring resonators, respectively.

Figure 3 Histogram of split ratios of six sets of ring resonators; each set contains seven rings with variable lengths but the same coupling gap and coupling length (the total number of resonances analyzed is around 1080). When a resonance splitting is larger than half of the 3 dB bandwidth, it becomes visible.

can explain this asymmetry in a satisfactory manner. Still, our experimental data shows that, in many cases, a significant fraction of the split resonances are asymmetrically split (see Fig. 4), making it necessary to build a fitting model which could handle all kinds of resonances. Another difficulty is the experimental identification and quantification of the different contributions to the backscattering and resonance splitting. So far, analysis of measurements on silicon microrings has attributed all backscattering to waveguide roughness distributed along the waveguide [10, 16]. The possible contribution to backreflection from the directional
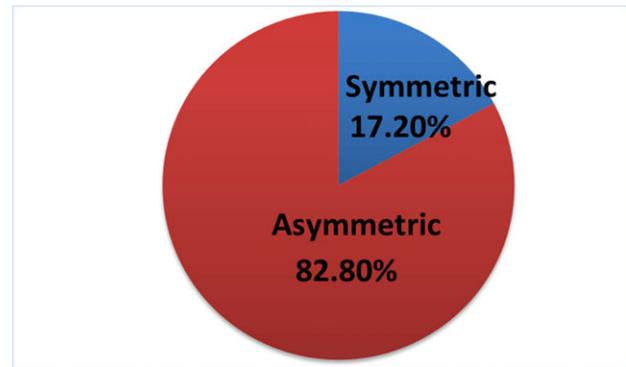

Figure 4 A pie chart clearly shows the prevalence of asymmetric ones among all of the splitting resonances from spectra of 252 measured rings (in total more than 550 resonances exhibit splitting).

couplers has only been theoretically proposed [17], but has not yet been experimentally verified and quantitatively characterized. In this paper, we develop a fitting model that can explain and reproduce all kinds of split and non-split resonances, and identify the origin of asymmetrically split resonances. Moreover, we propose and experimentally prove that, besides waveguide roughness, the directional couplers indeed contribute to backscattering in silicon microrings. The influence of the coupler's gap as well as extra coupling length on coupler-induced backscattering is also investigated.

In the following section, the theoretical analysis and the models for the individual contributions to backscattering are introduced; so is the model based on *temporal coupled mode theory* (t-CMT) for the ring with backscattering, with which all resonances can be fitted in a satisfactory manner. In section 3, the origin of asymmetry in most split resonances is identified, which is the backcoupling of couplers. Subsequently, the fitting results of measured ring spectra and experimental characterization of backscattering are presented in section 4, where the influences of coupler gap, ring length and coupling length on backscattering are also shown. We will then make our model more rigorous and complete by revealing the reason why individual resonances within the same spectrum can be so significantly different. In this section, the model will be improved by fitting the ring circuit and its whole spectrum instead of fitting the resonances one by one.

2. t-CMT model for a ring resonator

Temporal coupled-mode theory (t-CMT) is a very good and useful model to analyze a single resonance of a ring resonator [18]. The model presented in this paper improves upon existing models in that it includes both distributed and localized (lumped) backscattering: distributed backscattering is caused by waveguide sidewall roughness distributed along the ring circumference, while lumped backscattering

is caused by localized discontinuities in the ring. In most rings, these discontinuities can be found in the coupler.

In this section, the t-CMT model for the ring circuit with backscattering taken into consideration is first introduced. After that, the models and analysis for the individual contributions to backscattering, namely the directional couplers (lumped) and waveguide roughness (distributed), are discussed.

A perfect ring resonator supports two degenerate modes, *clockwise* (CW) propagating and *counterclockwise* (CCW) propagating, respectively. Ideally, only one of them is excited by its corresponding input. However, due to backscattering in the ring waveguide, these two modes can become coupled with each other and thus excited simultaneously, as shown in Fig. 1b. By introducing a lumped reflector with field reflectivity r_{bs} to represent backscattering, t-CMT can also be used to analyze a non-ideal ring resonator.

Equations (1)–(4) are based on our t-CMT model describing the two coupled resonance modes, and the transmission at the *drop* and *add* ports, respectively (the equations for the *in* and *pass* ports are similar):

$$\frac{d\alpha_{cw}}{dt} = j\left(\omega_0 + j\frac{1}{\tau_{tot}}\right)\alpha_{cw} - j\mu_{12}\alpha_{ccw} - j\mu_i S_i, \quad (1)$$

$$\frac{d\alpha_{ccw}}{dt} = j\left(\omega_0 + j\frac{1}{\tau_{tot}}\right)\alpha_{ccw} - j\mu_{21}\alpha_{cw} - j\mu_i' S_i, \quad (2)$$

$$S_d = -j\mu_o\alpha_{cw} - j\mu_o'\alpha_{ccw}, \quad (3)$$

$$S_a = -j\mu_o'\alpha_{cw} - j\mu_o\alpha_{ccw}. \quad (4)$$

Here

- α_{ccw} and α_{cw} are the amplitudes of these two modes, respectively [18].
- ω_0 is the intrinsic resonant frequency of the ring, depending on the ring's physical parameters.
-

$$\frac{1}{\tau_{tot}} = \frac{1}{\tau_l} + \frac{1}{\tau_i} + \frac{1}{\tau_o}$$

is the total decay rate of the ring circuit, including the intrinsic loss rate $1/\tau_l$ and out- and in-coupling rates $1/\tau_i$ and $1/\tau_o$. We can assume that the last two are identical if the two couplers are designed to be identical, as is often the case. The relation between decay rate and mutual coupling is [18]

$$\mu_x^2 = \frac{2}{\tau_x}. \quad (5)$$

- μ_i and μ_o are the mutual forward couplings of two directional couplers, respectively; the dependency on the power forward coupling coefficient in space $K = k^2$ is [18]

$$\mu_i^2 = \mu_o^2 = K_i\frac{v_g}{L} = K_i\frac{c}{n_g L}. \quad (6)$$

Here
- v_g is the group velocity in the ring circuit.
- L is the physical length of the ring.
- c is the light speed in vacuum.
- n_g is the group index of the ring.
- μ_{12}, μ_{21} refer to the mutual couplings of a lumped reflector inside the ring waveguide, which are used as a model for the backscattering. Based on the fact that the strength of the backscattering should be independent of the propagation direction, μ_{12}, μ_{21} are assumed to have the same amplitudes. However, they might have different phases due to the stochastic and distributed nature of the backscattering which is captured in a lumped element: the effective coupling positions for the two modes may be different, as also discussed in depth in [19], where a circuit model for backscattering that takes both amplitude and phase stochastic features into consideration is proposed. The dependency on field reflectivity r_{bs} is

$$\mu_{12} = r_{bs}\frac{v_g}{L} = r_{bs}\frac{c}{n_g L}. \quad (7)$$

In the wavelength domain the field reflectivity r_{bs} is also reported to show a stochastic nature [16, 19]. However, in our model, r_{bs} within one resonance is considered to be constant, due to the ultra-narrow bandwidth of a ring resonance, which is measured to be around 10–40 pm.
- μ_i' and μ_o' are related to the backcouplings of the coupler. Similarly to μ_i, the dependency on power backcoupling coefficient $K' = \mathbf{k}'^2$ is

$$\mu_i'^2 = \mu_o'^2 = K'\frac{v_g}{L} = K'\frac{c}{n_g L}. \quad (8)$$

For simplicity, a dimensionless factor f is introduced to mathematically describe the backcoupling k' relative to the forward coupling coefficient k:

$$k' = fk, \quad \mu_i' = f\mu_i. \quad (9)$$

Note that f can be complex, so there can be a phase difference between forward coupling and backcoupling.
- S_x refers to the amplitude of the wave at each port. It is normalized such that S_x^2 has the unit of power.

After solving equations (3) and (4), we get the amplitudes at the *drop* port S_d and *add* port S_a as equations (10) and (12). For comparison, the case without any backscattering is given as equations (11) and (13):

$$\frac{S_d}{S_i}\Big|_{bs} = \frac{A_d}{2}\left[\frac{\frac{BW_0}{2}(1-f)^2}{j(\omega-\omega_1) + \frac{BW_1}{2}} + \frac{\frac{BW_0}{2}(1+f)^2}{j(\omega-\omega_2) + \frac{BW_2}{2}}\right],$$
$$(10)$$

$$\frac{S_d}{S_i}\bigg|_{\text{ideal}} = A_0 \left[\frac{\frac{BW_0}{2}}{j(\omega - \omega_0) + \frac{BW_0}{2}} \right], \qquad (11)$$

$$\frac{S_a}{S_i}\bigg|_{\text{bs}} = \frac{A_a}{2} \left[-\frac{\frac{BW_0}{2}(1-f)^2}{j(\omega - \omega_1) + \frac{BW_1}{2}} + \frac{\frac{BW_0}{2}(1+f)^2}{j(\omega - \omega_2) + \frac{BW_2}{2}} \right], \qquad (12)$$

$$\frac{S_a}{S_i}\bigg|_{\text{ideal}} = 0. \qquad (13)$$

Here

- A_x is a dimensionless factor, scaled by potential transmission losses in the circuit. For ideal circuits, where no extra loss is present, $A_x = 1$.
- BW_0 is the 3 dB frequency bandwidth of the ring when there is no backscattering at all, i.e. an ideal ring.
- (ω_1, BW_1) and (ω_2, BW_2) are the (central frequencies, frequency bandwidths) of the CW resonance mode (α_{cw}) and CCW resonance mode (α_{ccw}), respectively.

Also

$$\omega_1 = \omega_0 + \mu_0 \cos\frac{\phi_\mu}{2}, \qquad (14)$$

$$\omega_2 = \omega_0 - \mu_0 \cos\frac{\phi_\mu}{2}, \qquad (15)$$

$$BW_1 = BW_0 + 2\mu_0 \sin\frac{\phi_\mu}{2}, \qquad (16)$$

$$BW_2 = BW_0 - 2\mu_0 \sin\frac{\phi_\mu}{2}. \qquad (17)$$

Here $\mu_0 = |\mu_{12}\mu_{21}|$ and $\phi_\mu = \angle\mu_{12}\mu_{21}$. ϕ_μ depends on the effective coupling position of the two circulating modes, and our fitting results show that ϕ_μ is close to 0; this means that $\phi_{\mu_{12}} = -\phi_{\mu_{21}}$: in other words, the positions where coupling between these two modes effectively happens are the same. What is more, this demonstrates that the coupling between the two modes is conservative rather than dissipative.

From equations (14)–(17), the distortion of the electric field at the *drop* port and the emergence of light at the *add* port, due to μ_{12} and f, are observed. Instead of a single resonance with a Lorentzian line shape, there are now two resonances with their own resonance frequency/wavelength, bandwidth and peak power. When the separation between the two resonance frequencies becomes sufficiently large compared to their bandwidth, a visible peak splitting can be observed.

Table 1 The detailed data of the above spectrum in Fig. 5. The existence of *f* can be inferred from a comparison of the first and third resonances. The peak with larger bandwidth has a higher peak power; comparing the first and second resonances, the relative difference in bandwidths of the first resonance is only 6.7%, whereas that in the second resonance is 31.6%, but the first one shows an even larger difference in peak power (47.5%) than the second one (42%); this decoupling of relative peak power and bandwidth can only be explained with a non-zero *f*.

	Resonance 1	Resonance 2	Resonance 3
BW_1/pm	16.7188	14.1098	21.0971
BW_2/pm	15.6252	19.4137	22.5090
$\frac{\Delta BW}{BW_0}$	6.76%	31.6%	6.47%
P_1	0.1447	0.1236	0.099
P_2	0.0892	0.0807	0.110
$\frac{\Delta P}{P_0}$	47.5%	42.0%	10.5%

Obviously, μ_{12} is responsible for the separation of the resonance frequencies, which is in agreement with models formerly published in [20]. In terms of the relative power in these two modes, there seems to be a dependency on both the bandwidth and the backcoupling factor f. The existence of backcoupling can thus be deduced from experimental data. Table 1 shows the characteristics of different split resonances from the same ring resonator. If there were no backcoupling at all ($f = 0$), the only reason that there could be an asymmetry in the peak power of the two modes is that their bandwidths are different, as can be seen in the denominator of equation (10). As a consequence, a larger bandwidth will lead to a lower peak power, and a large difference between peak power should correspond with a large difference in bandwidth. However, something different is observed in the measured spectra shown in Table 1. For the first and third resonances, the peak with the larger bandwidth actually has a higher peak power. In addition, when comparing the first and second resonances, we also find a discrepancy: in the first resonance, the two peaks have a much smaller difference in bandwidth (6.7%) than in the second resonance (31.6%), but at the same time the two peaks of the first resonance have a larger difference in power (47.5%) than those of the second one (42%). It is already explained that ϕ_μ is very close to 0, meaning that the difference in bandwidth can be very small. All of these phenomena reveal that, besides bandwidth, there must be another factor introducing an asymmetry.

This observation has been confirmed with t-CMT simulations in the circuit simulator *Caphe* [21, 22] by Luceda Photonics. When a ring resonator with backscattering, but without backcoupling in the directional coupler, is simulated, only symmetrically split resonances are obtained. After introducing backcoupling into the coupler model, the asymmetry in split resonances starts to emerge, as shown in Fig. 6.
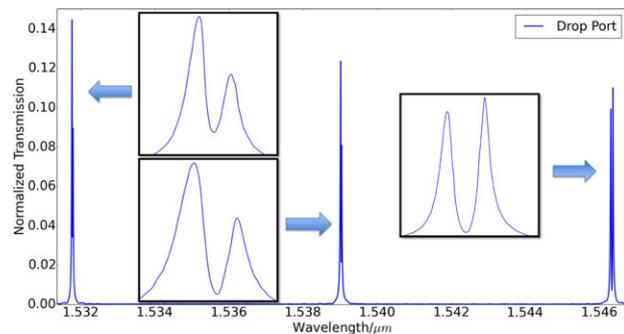
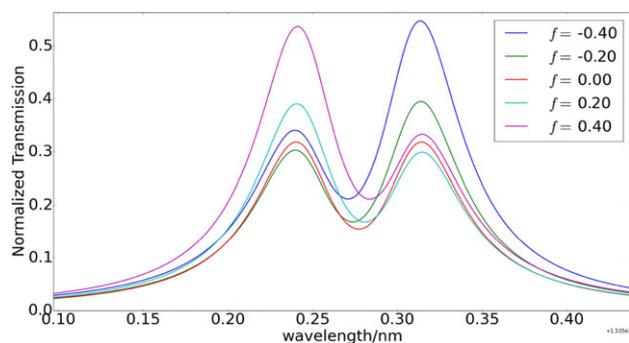**Figure 5** A measured spectrum with three split resonances.

Figure 6 A sweep of different f factors using circuit simulator Caphe. When $f = 0$ and $\phi_\mu = 0$, the red line is generated, which is a symmetric split resonance; when the magnitude of f is increased, the degree of asymmetry increases accordingly.

3. Individual contributions to backscattering

A ring resonator consists of a circular waveguide and one or two directional couplers. Each component can potentially introduce unwanted reflection or scattering, contributing to the total backscattering in the ring. These contributions will be discussed in more detail.

3.1. Sidewall roughness-induced backscattering

For the ring waveguide itself, roughness-induced backscattering is the only contribution to backscattering in the ring that has been verified and analyzed in detail. Other potential contributions from the ring waveguide could include the interface between a bend and a straight waveguide. In [23], the bend radius of a ring resonator is chosen to be as large as 20 μm. At such large radii, the transition between bend and straight waveguide is almost perfect in silicon wire waveguides [24], which might explain why only roughness-induced backscattering was observed. For sharper bend radii, 5 μm or even smaller, the interface between bend and straight section can introduce additional reflections.

According to [16], roughness-induced backscattering can be considered as a statistical process, where the reflectivity's spectral characteristics (mean value, standard deviation and correlation length) depend on the waveguide length. Using optical frequency-domain reflectometry (OFDR), Morichetti [16,25] demonstrated a linear relationship between reflected power R_w and waveguide length if the waveguide is short compared to the decay length of the propagation losses. For a ring resonator, the same technique clearly shows how a coherent addition of the reflections for each round trip in the ring increases the reflected power around the resonance wavelength. This linear relationship is

$$R_w = r_w^2 = H_w \times L_w. \tag{18}$$

Here H_w is a parameter dependent on waveguide dimension and sidewall quality.

3.2. Coupler-induced backscattering

In addition to the waveguide roughness, the directional couplers should also be considered as a source of backscattering. Ideally, a directional coupler shown in Fig. 1 c does not have any reflection r' and backcoupling k', leaving only forward coupling k and transmission t. But this is not always the case: the experimentally determined increase in loss in coupling sections [26] indicates that this reflection component can be non-negligible in microrings.

There can be two different types of backscattering associated to a directional coupler (Fig. 1 d).

1. The existence of an adjacent waveguide is actually a perturbation to the effective index of the original waveguide. So, the beginning and end interfaces of a directional coupler can behave like scatterers due to an abrupt change in effective index. This scattering can couple to the backward-propagating waveguide modes, i.e. an unwanted field backreflection r' to the input port and a backcoupling k' to the adjacent port. The more abrupt this transition from an isolated waveguide to a pair is, the stronger the scattering can be. The abruptness increases for a smaller gap, so we can expect a larger backscattering of the coupling sections in rings with a smaller gap.
2. For directional couplers with a long (straight) coupling section, the power is exchanged back and forth between the two waveguides, increasing the local field intensity at the internal walls, which is verified by a commercial finite-difference time-domain (FDTD) simulator provided by Lumerical, as illustrated in Fig. 7. Therefore, for the same waveguide length, there can be significantly higher backscattering by sidewall roughness compared to a single waveguide. The coupler roughness-induced backscattering is indicated as r_c. Similar to waveguides (equation (18)), the total reflected power $R_c = r_c^2$ has a form of

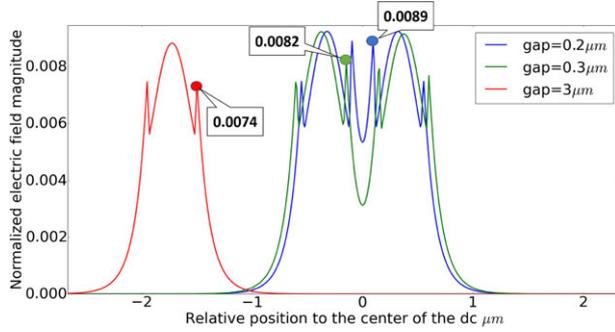$$R_c = H_c \times L_c, \text{ where } H_c > H_w. \tag{19}$$

Figure 7 FDTD simulations of mode profiles of directional couplers with 200 nm gap (blue) and 300 nm gap (green), as well as single-mode waveguide (red). Clearly, the electric field magnitude at the sidewall of a directional coupler is stronger than that of a waveguide.

3.3. Separation of distributed and lumped backscattering

In our t-CMT model for a ring resonator, both backscattering r_{bs} and backcoupling k' are included. The backscattering r_{bs} consists of distributed backscattering caused by waveguide roughness (r_w), whose power reflectivity has a linear dependence on ring length L, and lumped reflection introduced by couplers (r' and r_c), whose power reflectivity should be independent of ring length, but dependent on couplers' parameters, for instance, gap and coupling length. Based on this knowledge, assuming a low average total reflectivity during one round trip, only first-order reflection contributions are taken into account. When the ring length $L << 1/(2\alpha_{loss})$. we propose for low-field reflectivity r_{bs} a simple linear approximation of power reflectivity $R_{bs} = r_{bs}^2$:

$$R_{bs} = H_0 L + C_0. \tag{20}$$

Here $H_0 L$ refers to the distributed backscattering caused by roughness and C_0 covers the contribution from the couplers.

4. Experimental results

A set of rounded rectangular *add–drop* microrings (fixed 6.5 μm coupling length and 4.5 μm bend radius) with seven different total ring lengths (150–1000 μm) and six different coupling gaps (150–400 nm) were measured in order to verify the model proposed in equation (20). With this, we intend to verify that the sources of backscattering include circular waveguide roughness as well as directional couplers. All resonances between 1520 nm and 1560 nm are analyzed, using a 1 pm resolution wavelength scan with a continuous-wave tunable laser and a power meter in a vertical coupling setup. The devices were designed with the IPKISS framework [27] and fabricated at IMEC in a passive silicon photonics technology [28]. The waveguide
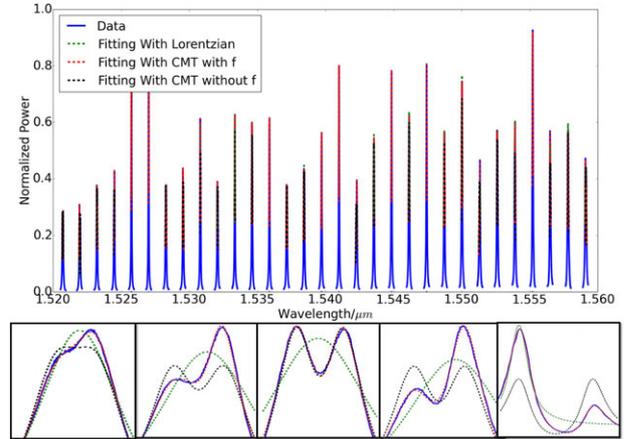

Figure 8 Comparison of fitting results using three different models. Measured data is shown in blue solid line; in green dashed line data it is fitted with traditional Lorentzian model. The black dashed line gives the fitting with the t-CMT model but without backcoupling factor *f*. Clearly, only symmetrically split resonances are correctly handled. The fitting results of the complete t-CMT model with *f* is shown in red dashed line, which closely matches the measurements.

dimensions are 450 nm × 220 nm, embedded in oxide and excited with TE polarization using fiber grating couplers.

4.1. Fitting

First of all, our model is verified by testing its capability to fit all the peaks of different ring resonators. Equation (10) is implemented into our Python modeling code and the parameters are fitted to the resonance spectrum of the *drop* port using a least-square algorithm. With small modifications, the same procedure can be applied to the *pass* port spectrum. The free parameters in the frequency domain are $[P_p, \omega_0, BW_0|_\omega, \mu_0, f, \phi_\mu]$, or similarly in the wavelength domain $[P_p, \lambda_0, BW_0|_\lambda, \mu_0, f, \phi_\mu]$, which correspond to [peak power, central frequency, 3 dB bandwidth, amplitude of backscattering, backcoupling factor, phase of backscattering], respectively. The values of P_p, ω_0 and $BW_0|_\omega$ correspond to the resonance of the ideal ring as if there was no backscattering present, while the other parameters μ_0, f and ϕ_μ describe the perturbation due to the backscattering.

Figure 8 gives examples of three different ring models. The green line is the result of a traditional Lorentzian model. It fails to fit resonances with even a small amount of splitting. The black line fits the resonances with a t-CMT model with backscattering, but without backcoupling ($f = 0$). Only symmetrically split resonances can be handled by this model, and it performs poorly for asymmetric peaks. Our improved t-CMT model with a non-zero backcoupling factor f is plotted in the red dashed line. It accurately fits non-split, symmetrically split and asymmetrically split resonances.

Figure 9 plots the f factor for a typical example of measured rings. The amplitude of the f factor varies from
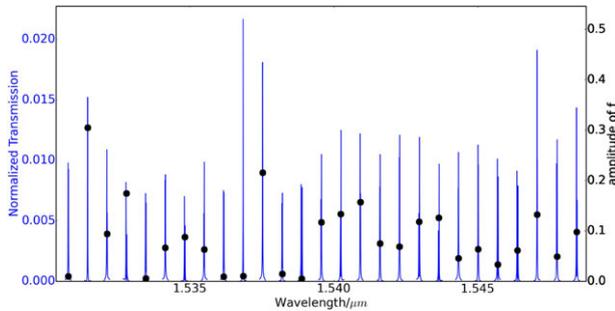
Figure 9 A measured spectrum with fitted amplitude of f factor at each resonance. Similarly in other measured spectra, the amplitude of f is in the range of 0 to 0.4.

0 to 0.4, which means that there can be as much as 40% of the cross-coupled field (16% of the power) coupled back to the adjacent port of the *in* port. Such a large value explains the significant difference in peak power in some split resonances.

4.2. Extracting the backscattering

With an accurate peak-fitting model we can now look deeper into the actual backscattering in silicon on insulator (SOI) microrings. First of all, the strength of the backscattering will be mathematically extracted from measured spectra. By analyzing the transmission spectra at the *drop* port and the *add* port, the field backreflectivity r_{bs} for each individual resonance can be calculated. As the r_{bs} variation with wavelength has a strong stochastic component, we look at the mean and standard deviation of r_{bs} over the different resonances within the transmission spectrum of a single ring. For resonances that are visibly split, r_{bs} is calculated as

$$R_{bs} = r_{bs}^2 = \mu_0^2 \frac{n_g L}{c} = \mu_0^2 \frac{\lambda_0^2}{c \times FSR_\lambda}, \quad (21)$$

where FSR_λ is the free spectral range in the wavelength domain and λ_0 is the central wavelength of the fitted resonance. All of these parameters, λ_0, FSR_λ and μ_0, can be directly extracted from the fit of the peak. From equations (14) and (15), equation (22) can be generated:

$$\Delta\omega_{bs} = \omega_1 - \omega_2 = 2\mu_0 \cos\frac{\phi_\mu}{2} = \frac{2\pi c}{\lambda_0^2}\Delta\lambda_{bs}. \quad (22)$$

And, as discussed in section 2, ϕ_μ is always very close to 0, it is further simplified as

$$\mu_0 = \frac{\pi c}{\lambda_0^2}\Delta\lambda_{bs}. \quad (23)$$

Now, in combination with equation (7), equation (24) can be generated:

$$\frac{\Delta\lambda_{bs}}{BW_\lambda} = \frac{\mathcal{F}r_{bs}}{\pi}. \quad (24)$$

Here $\Delta\lambda_{bs}$ refers to the wavelength spacing between the two peaks of a split resonance. $\mathcal{F} = FSR_\lambda / BW_\lambda$ is the finesse of the ring, where $\mathcal{F}/2\pi$ is the number of round trips light makes during the cavity lifetime. This equation mathematically describes the coherent addition of the back-reflection contribution for each of the $\mathcal{F}/2\pi$ round trips.

However, for non-split peaks, the fitted parameter μ_0 is not always reliable, as the effect of the envelope shape on the properties of the individual peaks can be ambiguous: there are often multiple solutions for the resonance modes α_{cw} and α_{ccw}. Instead, the relative peak intensity at the *add* and *drop* ports can be used to calculate r_{bs}. After some transformations of equations (10) and (12), we get

$$\frac{P_A}{P_D} = \frac{\left(\frac{\Delta\lambda_{bs}}{BW_\lambda}\right)^2}{1 + \left(\frac{\Delta\lambda_{bs}}{BW_\lambda}\right)^2} = \frac{\left(\frac{\mathcal{F}r_{bs}}{\pi}\right)^2}{1 + \left(\frac{\mathcal{F}r_{bs}}{\pi}\right)^2}. \quad (25)$$

Similar to equation (24), the dependency on $\mathcal{F}r_{bs}$ reflects the coherent addition of reflection per round trip at resonance.

4.3. Separating distributed and lumped backscattering

In equation (20), the total backscattering is separated into contributions by lumped scatterers (C_0) and by distributed scatterers (H_0), like sidewall roughness. H_0 depends on the electric field strengths at the sidewalls and the quality of the sidewalls. A lower value of H_0 can be obtained by using a better etch process, broader waveguides or the TM polarization [25, 29].

We applied our model and extraction procedures to rings with different round-trip lengths and coupling gaps. The propagation losses in the measured waveguides are of the order of < 2 dB/cm [8]. This makes, even if the additional losses in the coupling sections of small-gap resonators are considered, the linear approximation in equation (20) a valid assumption.

The power reflectivity R_{bs} is plotted in Fig. 10, which confirms that the highest power reflection R_{bs} per round trip is of the order of 0.01, and therefore higher order reflection contributions can indeed be safely neglected in equation (20).

It is clearly observable that that the reflected power increases linearly with the ring length, confirming the length-dependent model from equation (20). It is also shown that for a larger coupler gap, the curve shifts down. This confirms that the directional coupler plays an important role in the lumped scattering contribution C_0, and that smaller gaps will lead to stronger discontinuities and backscattering.
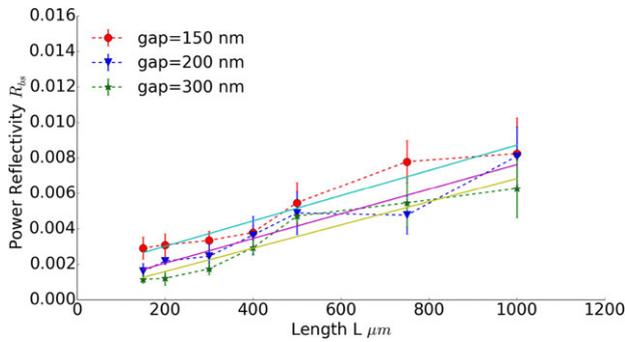
Figure 10 Power backscattering per round trip for rings with different round-trip lengths and different directional coupler gaps. A linear increase of the backscattering for longer rings is observed, which corresponds to the distributed scattering H_0. A decrease in backscattering for larger coupler gaps is also shown, corresponding to the lumped scattering C_0 in the directional couplers.
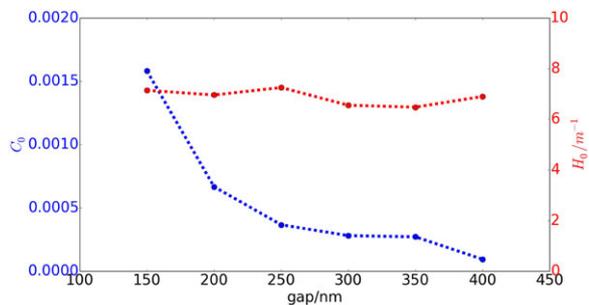

Figure 11 Fitted parameters H_0 and C_0 versus coupler gap. H_0 remains constant for different gaps, as it only depends on the ring waveguide roughness. And, the value is well matched with the formerly reported value. C_0 decreases for increasing gap, as the larger the gap is, the smaller the influence of the directional coupler will be.

This is again confirmed in Fig. 11, where dependences of C_0 and H_0 on the coupler gap are plotted. For all gaps, H_0 is quite stable around $6–8\,\mathrm{m}^{-1}$, which corresponds well with the value reported in [16]. As H_0 represents the backscattering caused by sidewall roughness, it is indeed expected to be independent of the gap. In terms of C_0, it is clearly shown in the same figure that rings with larger gap have smaller C_0, meaning less backscattering induced by the couplers.

4.4. Coupler-induced backscattering

C_0 is more complicated to understand than H_0. In reality, besides couplers the bend/straight transition might also introduce extra lumped reflections. These reflections could add a small contribution to C_0 that is independent of the coupling parameters. For simplicity, we assume that the lumped contributions to backscattering solely originate in the directional couplers. The effect of the couplers is investigated by measuring another set of rings with a fixed coupler gap (200 nm), seven different ring round-trip lengths (150–1000 μm) and six different coupling lengths (5–15 μm).
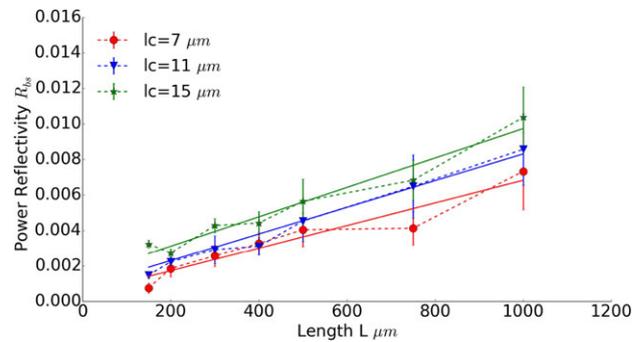

Figure 12 Power backscattering as a function of ring round-trip length for different coupling lengths L_c. The backscattering increases with larger round-trip lengths and with larger coupling lengths.
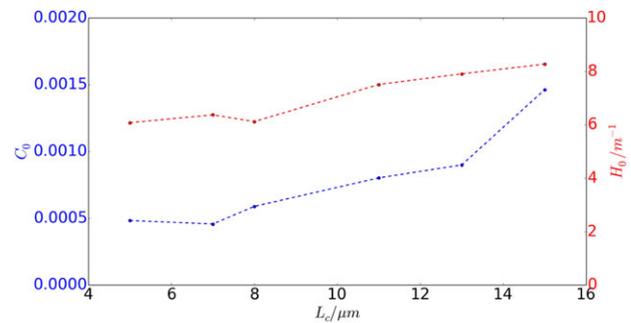

Figure 13 Fitted backscattering contributions H_0 and C_0 for different coupling lengths L_c. C_0 increases with increasing L_c, indicating more backscattering caused by directional couplers. H_0 remains in the expected range of 6–8 m^{-1}.

Figure 12 again plots R_{bs} as a function of ring length, but now for directional couplers with three different coupler lengths. The curves with the longer coupling lengths L_c show a higher backscattering. Figure 13 quantifies how C_0 increases with coupling length L_c. H_0 also shows a slight increase, but less pronounced, and still within the range reported in [16]. The change in H_0 can also be due to a secondary effect: longer coupler lengths increase the ring linewidth, which affects the quality of the fit due to the existence of noise in the spectrum.

All of the data shown tell us that the coupler sections indeed introduce considerable reflections, and the strength of those reflections depends on both gap and coupling length.

5. Wavelength-dependent model for full-spectrum fitting

With the model discussed in the previous section, we could accurately fit every individual resonance separately.

However, in reality, there should be a constant set of parameters for the ring circuit instead of a unique set of parameters for each resonance. Though, by claiming that each resonance has different parameters, i.e. backcoupling and backscattering, the differences between resonances in a

single spectrum could be explained. The question of how to physically explain the differences between these parameters still remains.

Back to our former analysis, we remind ourselves that there are two individual contributions: roughness-induced backscattering and directional couplers. It has already been reported in [16] that the roughness-induced backscattering exhibits a degree of randomness, which might be a reason for the different shapes of resonances in a single spectrum. However, our analysis and measurement results in previous sections reveal that the strength of backscattering only influences the spectral separation of the two split peaks. In other words, the large differences in peak powers of each split resonance cannot be explained by the randomness in backscattering.

When the layout of the system is considered, we see that for an add–drop filter, there are two couplers, so four scatterers in total. These four scatterers plus backscattering will form a complicated multi-cavity system in the ring circuit, which will show a certain wavelength dependency. In order to verify this, the circuit simulator Caphe with a detailed model for the ring circuit is used to fit the measured data. The fitting algorithm used is differential evolution[30], which is much more time consuming but rigorous than other simple algorithms like least square. The wavelength span of the fitting procedure as well as the measured spectrum is chosen to be 20 nm with a 1 pm resolution, in order to incorporate enough resonances and include adequate data points within a single resonance. In this model, a basic directional coupler contains two independent 'waveguides' corresponding with the even and odd supermodes. The effective indexes are simulated using FIMMWAVE. The scatterers at the input and output stages of a directional coupler couple the individual waveguide mode to the supermodes, and also add parasitic reflection and backcoupling. Thus, the parameters to be fitted include:

- coefficients of a third-order polynomial equation describing the effective index of the ring waveguide versus wavelength;
- coefficients of two second-order polynomial equations for the effective indexes of the two supermode waveguides;
- reflection and backcoupling of these scatterers. They are assumed to be constant among all of these scatterers;
- roughness-induced backscattering strength.

Moreover, for the sake of both accuracy and efficiency, we would prefer to implement a multi-stage fit, rather than a single fitting procedure that is fed with all parameters simultaneously. In detail, the effective index of the ring waveguide is first fitted to find the correct positions of the resonances. Then the effective indexes of the supermode waveguides are fitted to get the proper coupling strength of the directional couplers. Subsequently comes the fitting of these parasitics, including backscattering of the waveguide as well as backreflection and backcoupling of the scatterers.

Figures 14 and 15 show the fitting of two relatively short rings. Due to the limited number of resonances in the
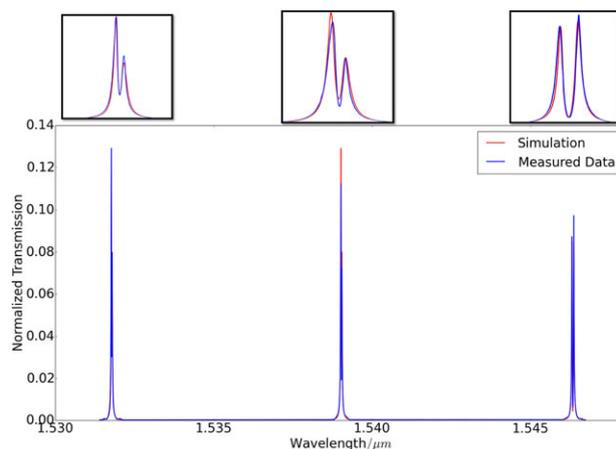

Figure 14 Fitting of a 75 μm long ring; here the circuit simulator Caphe is used to fit a ring circuit: in other words, the complete spectrum is fitted instead of individual resonances.
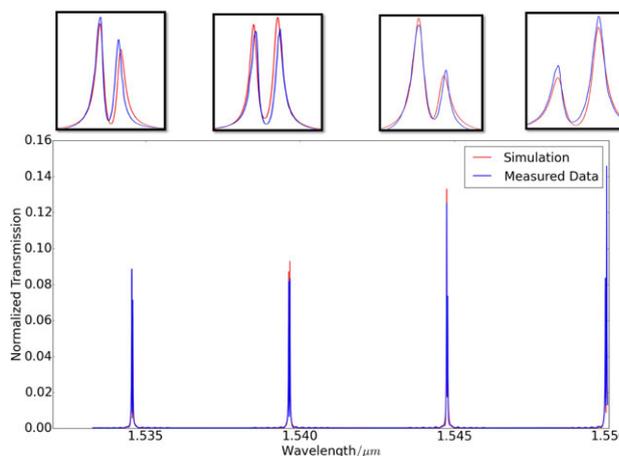

Figure 15 Fitting of a 100 μm long ring; the good matching shows the reproducibility of this circuit fitting model.

spectrum, the randomness of the backscattering does not play a significant role. Even if in our model backscattering is considered to be wavelength independent, a relatively good match between simulation and measured data can still be achieved, and the fitted parameters are consistent with previously fitting results or simulated values. For example, the power coupling ratio is of the order of 1×10^{-3}, similar to the value simulated by Lumerical FDTD Solutions, which is 3.6×10^{-3}. The fitted value of backcoupling of the directional coupler is of the order of 10^{-5}, in good correspondence with the previously reported f factor for the electric field, which is from 0 to 0.3, i.e. from 0 to 0.09 for power.

Figure 16 shows the fitting result of a longer ring, with more than 10 resonances. Due to the large number of resonances here, the randomness of the backscattering can become quite influential and will have an impact on the fitting quality. As expected, the fitting mismatch increases, which can actually be considered as a measure for
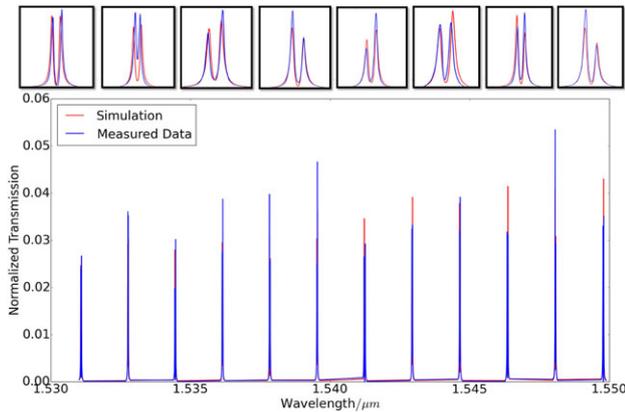
Figure 16 Fitting of a 300 μm long ring; larger mismatch is expected, due to the randomness of roughness-induced backscattering, which is not included in this circuit model. However, there is still a good match and it clearly shows the variety in split resonance shapes caused by multi-scatterers in the ring circuit.

randomness of the distributed backscattering. Still, we can extract trends from this fitting.

In summary, we identify two reasons in order to explain why individual resonances in the same ring can be quite different, not only in split ratio, but also in asymmetry and bandwidth. The first one is due to the previously reported randomness in waveguide-roughness-induced backscattering, and this will affect the split ratio of the resonances. The second contribution is from the complicated directional couplers, which contain not only lumped multi-scatterers that introduce extra reflection and backcoupling but also distributed backscattering due to the sidewall roughness of the extra coupling length.

6. Methods to suppress resonance splitting

After understanding the origin of the resonance splitting, a number of techniques to reduce or avoid resonance splitting can be suggested. Generally, the methods to suppress resonance splitting can be classified into four categories.

1. Improving the lithography and etching technology to reduce the sidewall roughness [25].
2. Using TM polarization or rib waveguides so that the sidewall sees a weaker electric field [25, 29].
3. Lowering the Q factor, i.e. strengthening the coupling coefficient of the directional coupler(s). Among the six measured sets of rings with gaps from 0.15 μm to 0.4 μm, there is a clear observable trend that resonance splitting is very rare in rings with a gap of 0.15 μm. On the other hand, rings with a gap larger than 0.25 μm almost invariably exhibit severe resonance splitting due to a narrower bandwidth/higher Q factor, as illustrated in Fig. 3.
4. Design optimization: either the backscattering r_{bs} or the backcoupling (f factor) of the whole ring circuit could be tailored. The former method relies on an

intentional reflector inside the ring, whose reflectivity as well as phase could be tuned, to compensate the parasitic backscattering r_{bs}. As a consequence, the total ring circuit can be made to suffer no backscattering at all. The second method tunes the f factor to be 1, so that the input wave contributes equally to CW and CCW modes. As in equation (10), when $f = 1$, one peak of a split resonance disappears. In such a case, the parasitic backscattering as well as the resonance splitting still occurs, but one peak is suppressed at the output.

7. Conclusions and outlook

This paper explains quantitatively the wide variation of resonance splitting in ring resonators. For this, a comprehensive and in-depth analysis of backscattering, one of the most severe as well as frequently observable problems in silicon microring resonators, is performed. It is based on measurements of abundant devices fabricated in mature CMOS technology. This quantitative analysis demonstrated the high probability of resonance splitting and the dominance of asymmetric ones in those resonance splittings. It also illustrated the problem of wide variations in resonance splitting of a single ring's spectrum.

In order to explain and model the resonance splitting (especially the asymmetric ones, which was hitherto impossible to model accurately), a model based on temporal coupled-mode theory is developed, which incorporates the parasitic processes of backscattering (distributed and lumped) as well as backcoupling in the coupler sections. The model is able to fit a wide variety of observed features, including single resonances and symmetrically and asymmetrically split resonances. Theoretical and experimental evidence that the origin of the asymmetry in split resonances is the backcoupling in the directional couplers are also presented. This model enabled us to get a deeper understanding of the mechanisms that contribute to backscattering in SOI microrings. The measurement results confirmed our hypothesis that backscattering is not only caused by sidewall roughness but also by the directional couplers. The relative influences of the coupler's gap and coupling length are also characterized in detail.

After successfully characterizing the splitting in a single ring resonance, our behavioral model is improved to explain the wide variations in resonance splitting within one spectrum. In this improved model, the directional coupler is modeled in a more rigorous way by decomposing it into multiple sections: two scatterers at the beginning and end sections that can introduce lumped reflection and backcoupling, and 'waveguides' with backscattering corresponding to the two supermodes in the directional coupler. The satisfying fitting results confirm that the very diverse cases of resonance splitting within one spectrum are indeed caused by the complicated multi-cavity system.

These models and characterization results will be valuable to improve the performance of silicon microring resonators and suppress the resonance splitting. Based on the work described here, future work will develop

different methods to suppress the resonance splitting or even the fundamental backscattering. Moreover, the model can also help to use the parasitic backscattering and resonance splitting for more useful purposes. Some work has already been done to utilize resonance splitting to design novel components or circuits, including integrated sensors, single-mode ring resonators, dual-wavelength laser cavities and even high-speed modulators.

References

[1] P. De Heyn, J. De Coster, P. Verheyen, G. Lepage, M. Pantouvaki, P. Absil, W. Bogaerts, J. Van Campenhout, and D. Van Thourhout, J. Lightwave Technol. **31**(16), 2785–2792 (2013).

[2] K. De Vos, I. Bartolozzi, E. Schacht, P. Bienstman, and R. Baets, Opt. Express **15**, 7610–7615 (2007).

[3] K. Vandoorne, P. Mechet, T. Van Vaerenbergh, M. Fiers, G. Morthier, D. Verstraeten, B. Schrauwen, J. Dambre, and P. Bienstman, Nature Commun. **5** (2014). DOI: 10.1038/ncomms4541.

[4] S. Gulde, A. Jebali, and N. Moll, Opt. Express **13**, 9502–9515 (2005).

[5] Q. Xu, V. R. Almeida, and M. Lipson, Opt. Lett. **30**, 2733–2735 (2005).

[6] H. Shao, H. Yu, X. Jiang, J. Yang, and G. Roelkens, IEEE 11th International Conference on Group IV Photonics (GFP) **4**, 47–48 (2014).

[7] T. Chu, N. Fujioka, and M. Ishizaka, Opt. Express **17**, 14063–14068 (2009).

[8] W. Bogaerts, P. De Heyn, T. Van Vaerenbergh, K. De Vos, S. Kumar Selvaraja, T. Claes, P. Dumon, P. Bienstman, D. Van Thourhout, and R. Baets, Laser Photon. Rev. **6**, 47–73 (2012).

[9] J. Heebner, R. Grover, and T. Ibrahim, Optical Microresonators: Theory, Fabrication and Applications, 1st ed., Springer Series in Optical Sciences (Springer, Germany, 2008).

[10] B. E. Little, J. P. Laine, and S. T. Chu, Opt. Lett. **22**, 4–6 (1997).

[11] S. Werquin, S. Verstuyft, and P. Bienstman, Opt. Express **21**(14), 16955–16963 (2013).

[12] M. Moresco, M. Romagnoli, S. Boscolo, M. Midrio, M. Cherchi, E. S. Hosseini, D. Coolbaugh, M. R. Watts, and B. Dutt, Opt. Express **21**(5), 5391–5400 (2013).

[13] Z. Zhang, M. Dainese, L. Wosinski, and M. Qiu, Opt. Express **16**, 4621–4630 (2008).

[14] G. C. Ballesteros, J. Matres, J. Mart, and C. J. Oton, Opt. Express **19**(25), 24980–24985 (2011).

[15] S. Tallur and S. A. Bhave, Opt. Express **21**(23), 27780–27788 (2013).

[16] F. Morichetti, A. Canciamilla, and A. Melloni, Opt. Lett. **35**, 1777–1779 (2010).

[17] J. Čtyroký, I. Richter, and M. Sior, Opt. Quantum Electron. **38**(9–11), 781–797 (2007).

[18] B. Little, S. Chu, H. Haus, J. Foresi, and J. P. Laine, J. Lightwave Technol. **15**(6), 998–1005 (1997).

[19] D. Melati, A. Melloni, and F. Morichetti, Adv. Opt. Photon. **6**(2), 156–224 (2014).

[20] M. A. Popović, Theory and Design of High-Index-Contrast Microphotonic Circuits, Ph.D. thesis (2008).

[21] M. Fiers, T. V. Vaerenbergh, K. Caluwaerts, D. V. Ginste, B. Schrauwen, J. Dambre, and P. Bienstman, J. Opt. Soc. Am. B **29**(5), 896–900 (2012).

[22] T. Van Vaerenbergh, M. Fiers, J. Dambre, and P. Bienstman, Opt. Quantum Electron. **47**(6), 1471–1476 (2015).

[23] F. Morichetti, A. Canciamilla, M. Martinelli, A. Samarelli, R. M. De La Rue, M. Sorel, and A. Melloni, Appl. Phys. Lett. **96**(May), 13–15 (2010).

[24] W. Bogaerts, P. Dumon, D. V. Thourhout, D. Taillaert, P. Jaenen, J. Wouters, S. Beckx, V. Wiaux, and R. G. Baets, IEEE J. Sel. Top. Quantum Electron. **12**(6), 1394–1401 (2006).

[25] F. Morichetti, A. Canciamilla, C. Ferrari, M. Torregiani, A. Melloni, and M. Martinelli, Phys. Rev. Lett. **104**(3), 033902 (2010).

[26] F. Xia, L. Sekaric, and Y. A. Vlasov, Opt. Express **14**(9), 3872–3886 (2006).

[27] M. Fiers, E. Lambert, S. Pathak, B. Maes, P. Bienstman, W. Bogaerts, and P. Dumon, J. Comput. Sci. **4**(5), 313–324 (2013).

[28] S. K. Selvaraja, P. Jaenen, W. Bogaerts, D. Van Thourhout, P. Dumon, and R. Baets, J. Lightwave Technol. **27**(18), 4076–4083 (2009).

[29] P. J. De Heyn, B. Kuyken, D. Vermeulen, W. Bogaerts, and D. Van Thourhout, High-performance low-loss silicon-on-insulator microring resonators using TM-polarized light, in: Optical Fiber Communication Conference (2011), p. OThV2.

[30] P. Rocca, G. Oliveri, and A. Massa, IEEE Antennas Propag. Mag. **53**(1), 38–49 (2011).